



# Numerical Study to Examine the Effect of Porosity on In-Flight Particle Dynamics

S. Kamnis, S. Gu, and M. Vardavoulias

(Submitted September 14, 2010; in revised form November 9, 2010)

**High velocity oxygen fuel (HVOF) thermal spray has been widely used to deposit hard composite materials such as WC-Co powders for wear-resistant applications. Powder morphology varies according to production methods while new powder manufacturing techniques produce porous powders containing air voids which are not interconnected. The porous microstructure within the powder will influence in-flight thermal and aerodynamic behavior of particles which is expected to be different from fully solid powder. This article is devoted to study the heat and momentum transfer in a HVOF sprayed WC-Co particles with different sizes and porosity levels. The results highlight the importance of thermal gradients inside the particles as a result of microporosity and how HVOF operating parameters need to be modified considering such temperature gradient.**

**Keywords** CFD, HVOF, in-flight, porous powder, WC-Co

## 1. Introduction

High velocity oxygen fuel (HVOF) thermal spraying has been applied successfully in producing coatings with higher density, superior bond strengths, and less decarburization due to its unique output of high particle velocities and relatively low particle temperatures. In the HVOF process, oxygen and fuel are mixed and burnt in a combustion chamber at high flow rates (up to 1000 L/min) and pressures (up to 12 bar) to produce a hot high-speed gas jet. Powder particles, normally in the size range 5–65  $\mu\text{m}$ , are injected into the gas jet where they are heated and accelerated toward the substrate. On impact the particles form lenticular splats, which adhere well to the substrate and to one another. The HVOF gun is scanned cross the substrate to build up the required coating thickness in a number of passes. The impingement and deformation of thermally sprayed particles have been investigated using CFD (Ref 1–3) and FEA (Ref 4–6) methods. Numerical models have also been developed to study the in-flight particle behavior during thermal spraying. Euler-Lagrange method is the most widely adopted approach for modelling of particle-gas interaction in various HVOF thermal spray systems. In the material aspects, there is a growing interest in deposition of WC-Co materials. As a class of hard

S. Kamnis and M. Vardavoulias, PyroGenesis S.A., Technological Park of Lavrio, 19500 Lavrio, Greece; S. Gu, School of Engineering Science, University of Southampton, Highfield, Southampton SO17 1BJ, UK; and S. Gu, Department of Civil Engineering, Xi'an Jiaotong-Liverpool University, No.111 Ren'ai Road, Suzhou Dushu Lake Higher Education Town, Suzhou 215123, Jiangsu Province, China. Contact e-mails: s.gu@soton.ac.uk and sai.gu@xjtlu.edu.cn.

### List of Symbols

$C_D$	Drag coefficient
$C_p$	Particle specific heat capacity, $\text{J} \cdot \text{kg}^{-1}/\text{K}$
$D$	Barrel diameter, m
$d_p$	Particle diameter, m
$F_D$	Drag force per unit particle, N
$f$	Solid fraction
$h$	Convective heat transfer coefficient, $\text{W} \cdot \text{m}^{-2}/\text{K}$
$H_{sf}$	Latent heat, J/kg
$\lambda_g$	Thermal conductivity of air in the pores, $\text{W} \cdot \text{m}^{-1}/\text{K}$
$\lambda_p$	Effective thermal conductivity, $\text{W} \cdot \text{m}^{-1}/\text{K}$
$\lambda_s$	Thermal conductivity of solid matrix, $\text{W} \cdot \text{m}^{-1}/\text{K}$
$k_c$	Partition coefficient
$Pr$	Prandtl number, $c_p \mu / K_\infty$
$Re$	Reynolds number based on particle diameter
$St$	Stokes number
$r$	Particle radius
$T$	Temperature, K
$T_L$	Liquidus temperature, K
$T_S$	Solidus temperature, K
$T_k$	Primary element melting temperature, K
$T$	Time, s
$u_p$	Particle velocity, m/s
$u_g$	Gas velocity, m/s

### Greek Symbols

$\alpha$	Thermal diffusivity, $\text{m}^2/\text{s}$
$\mu_g$	Gas viscosity, $\text{kg} \cdot \text{m}^{-1}/\text{s}$
$\rho_p$	Particle density, $\text{kg}/\text{m}^3$
$\rho_g$	Gas density, $\text{kg}/\text{m}^3$
$\rho_a$	Air density, $\text{kg} \cdot \text{m}^{-3}$
$\phi$	Shape factor
$\psi(T)$	Correction function
$\Delta t$	Time step, s
$\Delta r$	Grid node distance, m

composite materials of great technological importance, WC-Co powder cemented carbides can be used for protective coatings in a large variety of applications such as mining, turning, cutting, and milling, where abrasion, erosion, and other forms of wear exist. An excellent review on modelling, control and applications of HVOF thermal spray can be found in Ref 7. HVOF has been used successfully on spraying WC-Co materials. Considering a typical deposition rate of ~50% for HVOF process, there is a good scope for process optimization and efficiency improvement, which requires a clear understanding of the intricate interaction between process parameters and particle in-flight dynamics. The most relevant work for WC-Co and Ni particle dynamics has been done by Li et al. (Ref 8-10), who examined the in-flight particle behavior in a gas fuelled Diamond Jet hybrid HVOF system. The current technology trend is to use more cost-effective liquid fuelled HVOF system, which gives shorter particle residence times in the flame and lower temperatures. In our previous publication (Ref 11), a detailed study is reported to examine the morphological character of WC-Co powders and its effect on in-flight particle dynamics from a liquid fuelled HVOF gun. Modern methods of powder manufacturing, such as spray drying or self-propagating high-temperature synthesis (Ref 12) produces powder containing air voids which are not interconnected. Porosity influences the thermal transport properties of powder, while the heat flux from the HVOF gas flow to the particle is hampered by the porous structure, which inevitably influences the particle temperature. Moreover, the particle becomes lighter with porosity and is accelerated more by the gas flow, which will influence the impact velocity. This new study is to further develop the previous in-flight particle model to include the effect of microporosity of particles. The CFD model is used to examine the motion and heat transfer history of the in-flight particles of different sizes and porosity levels.

## 2. Mathematical Models

### 2.1 Momentum Transfer Equations

The acting forces on the particle could involve drag force, force due to pressure gradients, force due to added mass, Basset history term, and external potential forces (Ref 13). However, among the factors that affect particle movement during the HVOF process, only the drag force plays a dominant role, other factors can be neglected in most cases (Ref 13). Consequently, the governing equation for the motion of particles can be written as a force balance between the droplet inertia and the forces acting on the droplet, leading to:

$$\frac{du_p}{dt} = F_D(u_g - u_p) \quad (\text{Eq 1})$$

The drag force per unit particle mass is:

$$F_D = \frac{18\mu_g C_D Re}{\rho_p d_p^2} \quad (\text{Eq 2})$$

where the drag coefficient  $C_D$  is given by Morsi (Ref 14):

$$C_D = \frac{24}{Re} \left( 1 + b_1 Re^{b_2} \right) + \frac{b_3 Re}{b_4 + Re} \quad (\text{Eq 3})$$

$$b_1 = \exp(2.3288 - 6.4581\phi + 2.4486\phi^2)$$

$$b_2 = 0.0964 + 0.5565\phi$$

$$b_3 = \exp(4.905 - 13.8944\phi + 18.4222\phi^2 - 10.2599\phi^3)$$

$$b_4 = \exp(1.4681 + 12.2584\phi - 20.7322\phi^2 + 15.8855\phi^3) \quad (\text{Eq 4})$$

Here, the Reynolds number is defined by

$$Re = \frac{\rho_g |u_g - u_p| d_p}{\mu_g} \quad (\text{Eq 5})$$

As the gas flow is turbulent during HVOF spraying, the influence of the turbulence on particle behavior needs to be evaluated. The effect of turbulent fluctuation on particle aerodynamic response can be reflected by the Stokes number ( $St$ ), defined as the ratio of aerodynamic response time to the time scale associated with larger-scale turbulent eddies:

$$St = \frac{\rho_p d_p^2 u_p}{18\mu_g D}$$

Large Stokes numbers ( $St \gg 1$ ) mean slow response from the particle to large turbulent eddies. In our case of study, 10  $\mu\text{m}$  particles will be the lower limit for sprayed WC-Co powder which has a Stokes number of over 200 under the present HVOF flow conditions. That implies that the turbulence would not have a substantial effect on the behavior of such particles.

### 2.2 Heat Transfer Equations

The study of heat transfer in a thermal spray process (Ref 15) demonstrates that the transfer of heat by radiation from the surroundings to the particle is negligible when compared to convective heat flux from the gas to the particle. Consequently, the governing equation for particle heat transfer expressed in spherical coordinates is given by:

$$\rho_p C_p \frac{\partial T}{\partial t} = \lambda_p \left( \frac{\partial^2 T}{\partial r^2} + \frac{2}{r} \frac{\partial T}{\partial r} \right) + H_{sf} \rho_p \frac{df}{dt} \quad (\text{Eq 6})$$

Equation 6 can be written as:

$$\frac{\partial T}{\partial t} = \frac{\alpha}{\psi(T)} \left( \frac{\partial^2 T}{\partial r^2} + \frac{2}{r} \frac{\partial T}{\partial r} \right) \quad (\text{Eq 7})$$

where the function  $\psi(T)$  is defined as (Ref 16):

$$\psi(T) = \begin{cases} \text{if } T_S \leq T \leq T_L & 1 + \frac{H_{sf}(T_k - T_L)^{\frac{1-kc}{1-kc}}}{C_p(1-kc)(T_k - T)^{\frac{2-kc}{1-kc}}} \\ \text{else} & 1 \end{cases}$$

Here,  $T_k$  is the melting temperature of the primary element and  $k$  is the ratio between solid and liquid concentrations. Note that the above computational model assumes an infinite velocity for diffusion (equilibrium

condition) in the liquid phase and zero velocity in the solid (Ref 17). The boundary conditions associated with Eq 7 are specified separately on the surface and in the center of the particle, as:

$$\left. \frac{\partial T}{\partial r} \right|_{r=0} = 0; \quad \lambda_p \left. \frac{\partial T}{\partial r} \right|_{r=R} = h(T_g - T_R) \quad (\text{Eq 8})$$

where  $R$  represents the radius of the simulated particle,  $\lambda_p$  is the effective thermal conductivity of particle,  $T_g$  is the gas temperature, and  $h$  is the convective heat transfer coefficient. The heat transfer coefficient is evaluated using the Ranz and Marshall correlation (Ref 18):

$$Nu = (2 + 0.6Re^{1/2}Pr^{1/3}) \quad (\text{Eq 9})$$

where  $Nu$  is the Nusselt number, defined as:

$$Nu = \frac{hd_p}{k_g} \quad (\text{Eq 10})$$

The discretized form of Eq 7 is:

$$\alpha \frac{\Delta t}{\Delta^2 r} (i^{-1} - 1) T_{i-1}^{n+1} + \left( 2\psi_i^n + 2\alpha \frac{\Delta t}{\Delta^2 r} \right) T_i^{n+1} - \alpha \frac{\Delta t}{\Delta^2 r} (i^{-1} + 1) T_{i+1}^{n+1} = \alpha \frac{\Delta t}{\Delta^2 r} (1 - i^{-1}) T_{i-1}^n + \left( 2\psi_i^n - 2\alpha \frac{\Delta t}{\Delta^2 r} \right) T_i^n + \alpha \frac{\Delta t}{\Delta^2 r} (i^{-1} + 1) T_{i+1}^n \quad i = 1, 2, \dots, N - 1 \quad (\text{Eq 13})$$

where  $N$  is the number of discretization points along the radius of the droplet and  $n$  is time index. After a careful grid sensitivity analysis to all particle sizes, the nodal points are set to 10. For larger particles more discretization points may be required to improve the accuracy of the simulated melting and solidification kinetics. In the same manner, Eq 8 becomes:

$$-T_{N-1}^{n+1} + \left( 1 - \frac{h^n \Delta r}{k_i^n} \right) T_N^{n+1} = \frac{h^n \Delta r}{k_i^n} T_g \quad (\text{Eq 14})$$

Equation 7 in the center ( $r=0$ ) becomes indeterminate, implying that the relation in Eq 13 will not be applicable. By applying the theorem of L'Hospital, it is found that:

$$\frac{\partial T}{\partial t} = 3 \frac{\alpha}{\psi(T)} \frac{\partial^2 T}{\partial r^2} \quad (\text{Eq 15})$$

The discretized form of Eq 15 is:

$$\begin{aligned} & \left( \psi_0^n + 3\alpha \frac{\Delta t}{\Delta^2 r} \right) T_0^{n+1} - 3\alpha \frac{\Delta t}{\Delta^2 r} T_1^{n+1} \\ & = \left( \psi_0^n - 3\alpha \frac{\Delta t}{\Delta^2 r} \right) T_0^n + 3\alpha \frac{\Delta t}{\Delta^2 r} T_1^n \end{aligned} \quad (\text{Eq 16})$$

At each time step the algebraic system of Eq 13, 14, and 16 is solved using the Gauss Seidel iterative method, which is implemented as a user defined function in the numerical simulation with Fluent. The simulation time step is set to  $10^{-6}$  s and the convergence condition to  $10^{-4}$ .

### 2.3 Porosity Model

The microporosity of particles exerts its influence on effective thermal conductivity and particle density.

Although gases are among the poorest heat conductors, by themselves they do not constitute the best heat insulators. When the linear dimensions of a gas-filled space exceed approximately 1 cm, convection makes a large contribution to the total heat transfer across the space, at high temperatures radiation also becomes important. The best heat insulators are therefore solids which contain a high percentage of gas (usually air) in such a way that the individual gas spaces are small enough that convective heat transfer across them is negligible. These include porous powder and fibrous materials. The effective thermal conductivity of such composite gas-solid materials could be calculated from the properties and volume fractions of the component substances. Unfortunately, the conductivity of a composite material of known composition cannot be arrived at by any simple law of addition of the conductivities of its components. An approximation for effective thermal conductivity in the case of pores distributed in a solid, the formula of Maxwell and Rayleigh reads:

$$\lambda_p = \frac{\lambda_s}{1 + P \left( \frac{\lambda_s}{\lambda_g} - 1 \right)} \quad (\text{Eq 17})$$

where  $\lambda_s$  is the thermal conductivity of the solid matrix,  $\lambda_g$  is the proportional of the thermal conductivity of the air in the pores, and  $P$  is the porosity  $P = \frac{(\rho_s - \rho_p)}{(\rho_s - \rho_a)}$ .

The above formula assumes that convection through the pores is neglected, which is reasonable for not interconnected porous microstructure of low porosity such as in this study. Furthermore, the developed model assumes that the porous microstructure of the particles retains its size and structure during spraying. This is a reasonable assumption in the case of HVOF sprayed WC-Co powder, since melting is limited to fine particles ( $<5 \mu\text{m}$  size) based on our previous study (Ref 19).

## 3. Results and Discussions

The simulation is carried out as illustrated by the flowchart in Fig. 1. The calculation of 3-d combusting gas flow from the HVOF gun has been described thoroughly in Ref 20. To keep consistency with our previous work (Ref 11), the same WC-12Co powder is used. In this new study, the particles are given diameter of 10, 40, and 60  $\mu\text{m}$  and porosity of  $P=0, 3,$  and  $6\%$ . The thermophysical data used in the calculations are listed in Table 1. The particle loading allows the governing equations of gases and particles to be solved separately, in that case, the gas flow is simulated first and then particle dynamics is calculated

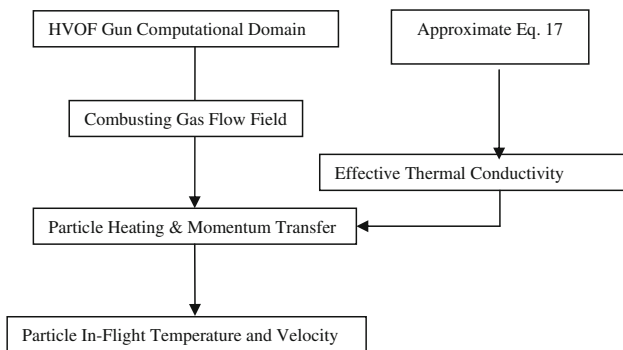


Fig. 1 Modelling approach

Table 1 Properties for WC-Co powder (Ref 19)

Density ( $\rho_p$ ), kg/m <sup>3</sup>	14,000
Solidus temperature ( $T_S$ ), K	1580
Liquidus temperature ( $T_L$ ), K	1640
Primary element melting point ( $T_K$ ), K	1768
Partition coefficient ( $k_c$ )	0.3
Specific heat ( $C_p$ ), J · kg <sup>-1</sup> /K	295
Latent heat ( $H_{sf}$ ), J/kg	420,000
Thermal conductivity ( $k$ ), W · m <sup>-1</sup> /K	15

through the established gas flow. The computational domain, detailed grid description and boundary condition can be found in Ref 20.

### 3.1 Porosity Influence on Velocity

Figure 2 shows the predicted axial velocities of particles with different sizes and porosities. Upon entering the gas field, the particles are accelerated by the gas in the gun's barrel. The injection is radial from two antipodal inlets attached on the barrel's wall 0.1 m away from the O/F inlets in the combustion chamber. It is evident from Fig. 2 that the particle size has a strong influence on the particle acceleration during the entire trajectories. The maximum velocity of the 10  $\mu\text{m}$  particle (~900 m/s) is almost three times higher than that of larger 60  $\mu\text{m}$  particles (~300 m/s). This variation in velocity is equivalent to a kinetic energy per unit mass of the impinging particle, which is one order of magnitude different. At this particle range it is worth noticing that the velocities of particles do not vary greatly with distance downstream to the gun exit after 0.2 m; a characteristic, that otherwise makes difficult to control the deposition parameters. The influence of porosity on particle acceleration is also illustrated in the same plot. The porosity changes the force balance in Eq 2 through the reduction of density from 14000 (zero porosity) to 13000 kg/m<sup>3</sup> (6% of porosity). This reduction in density influences the particle's inertia and consequently particle's acceleration. However, the difference at this low porosity levels is not significant to alter the particle velocity profiles or subsequently influence the deposition efficiency or deformation conditions as splats are being formed. A more quantitative comparison can be found in Table 2 for particle velocity at stand-off distance of 0.3.

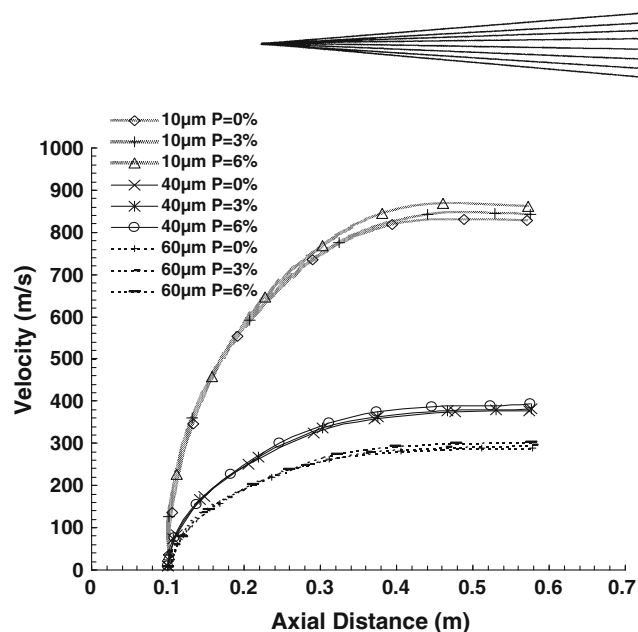


Fig. 2 Influence of porosity on particle's velocity

Table 2 Particle velocity (m/s) at impact

Particle porosity, %	Particle diameter, $\mu\text{m}$		
	10	40	60
0	832	375	290
3	845	383	296
6	870	390	300

It further confirms that the porosity range only has a marginal influence on particle acceleration in particular for large particles.

### 3.2 Porosity Influence on Temperature

A general assumption which has been widely accepted for HVOF sprayed particles is that temperature gradient within particles can be conveniently neglected. The temperature difference between the surface and the center of the particle is negligible indicating very small temperature gradients within the particle and almost uniform heating across the particle radius. The results for  $P=0\%$  in Fig. 3(a) confirm such assumption when the Biot number for the sprayed particles is  $<0.1$ . Nevertheless, when microporosity presents, the effective thermal conductivity changes according to porosity level, as a result, the temperature gradient becomes noticeable. Figure 3 shows the temperature plots on particle's surface and center for different size and porosity. For fully solid particles, as mentioned earlier, temperature gradient is almost zero throughout the range of particle size of  $P=0\%$ . The temperature gradient within the particle clearly develops according to porosity level and more pronounced for large particles. It needs to be noted that the maximum surface temperature of 60  $\mu\text{m}$  powder reaches 900 K for porous particles compared to 600 K for fully sold particles.

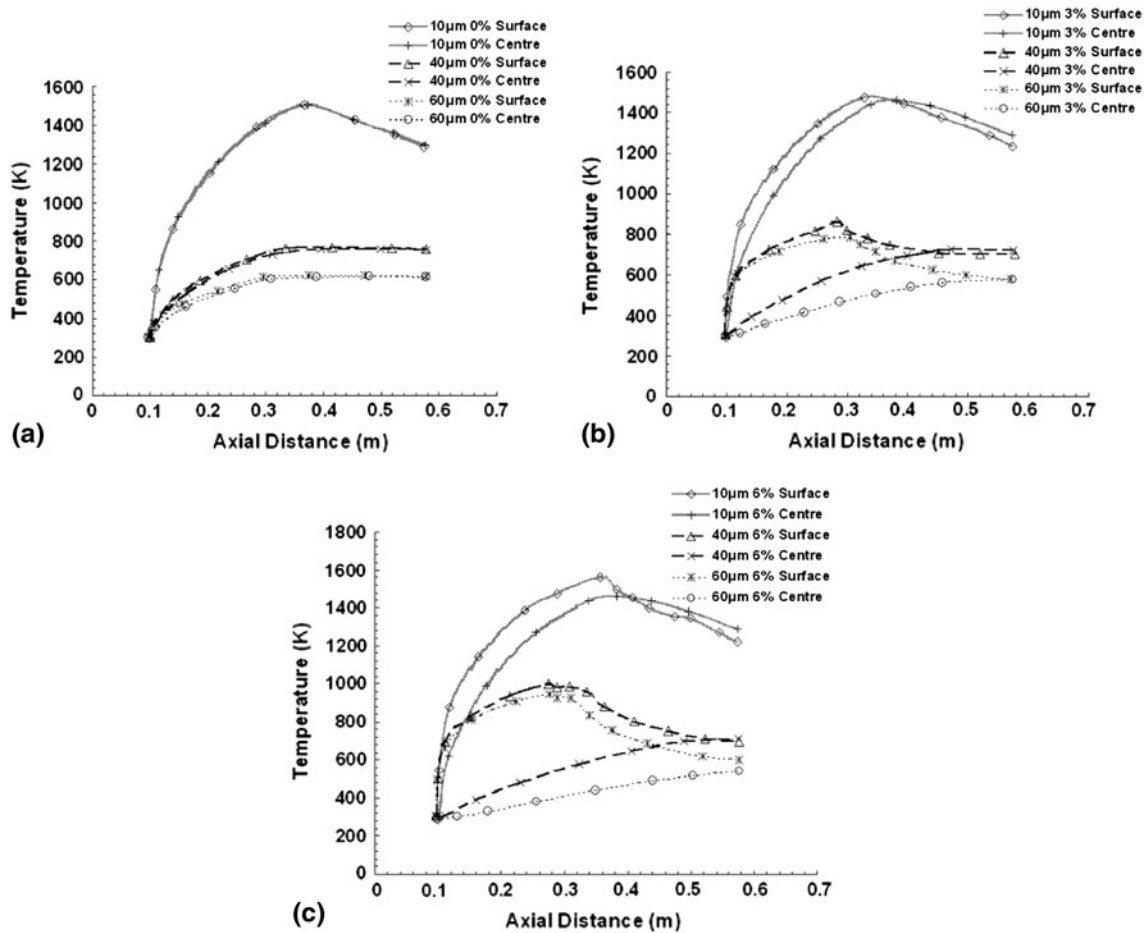


**Fig. 3** Surface and center temperature plots along particle trajectory

The difference of surface temperature is attributed to the limited thermal diffusion from surface to center and vice versa. Heat is transferred to particle surface through convection by the ambient gas flow, and then the heat is transferred to the particle center through conduction. The low thermal conductivity of air voids in porous particles slows down the heat transfer within the particles, as a result, more heat is retained close the surface to increase the temperature around. A very interesting phenomenon is observed for small particles of 10  $\mu\text{m}$  which are heated the highest temperature by the gas flow among all the particles. From 0.3 m onwards, the particle has higher temperature than the gas flow and starts to cool down. However, the porous structure reduces the thermal conduction to such extent that the surface temperature is lower than the core. The large particles have much lower temperature profiles and the core temperature have never reached the surface temperature during their residence time. Although the previous phenomenon does not exist for large particles, the structure of microporosity still has substantial effect on big particles as discussed below.

In Fig. 4, the temperature profiles inside 60  $\mu\text{m}$  particles are plotted along the particle radius at different in-flight distance from the injection point. This comparison

aims to underline the influence of porosity on the temperature gradient within a particle. For fully solid particles, the temperature profiles are straight lines from surface to center, indicating a uniform temperature distribution within the particle throughout the residence time. By increasing the microporosity, the effective thermal conductivity is reducing and consequently temperature gradients within the particle are developed. In the case of  $P=6\%$  it is clearly shown that the large gradient development is altering completely the thermal in-flight behavior of the particle. In the initial heating stage ( $x=0.1$  m), surface temperature increases rapidly to 540 K, while the center of the particle remains in the initial temperature of 300 K. At  $x=0.2$  m, the surface-center difference is rising to 540 K which is so significant difference that could have big influence on the deposition and deformation level of the particle upon impact on the substrate. This is due to an increase in thermal softening of the contacting surfaces upon impact, while plastic deformation is promoted due to increased strain rates as explained in our previous study on particle impingement (Ref 6). By comparing the three plots of Fig. 4, it is confirmed that porosity influences the particle heating from the surrounding gases and particularly porosity results in

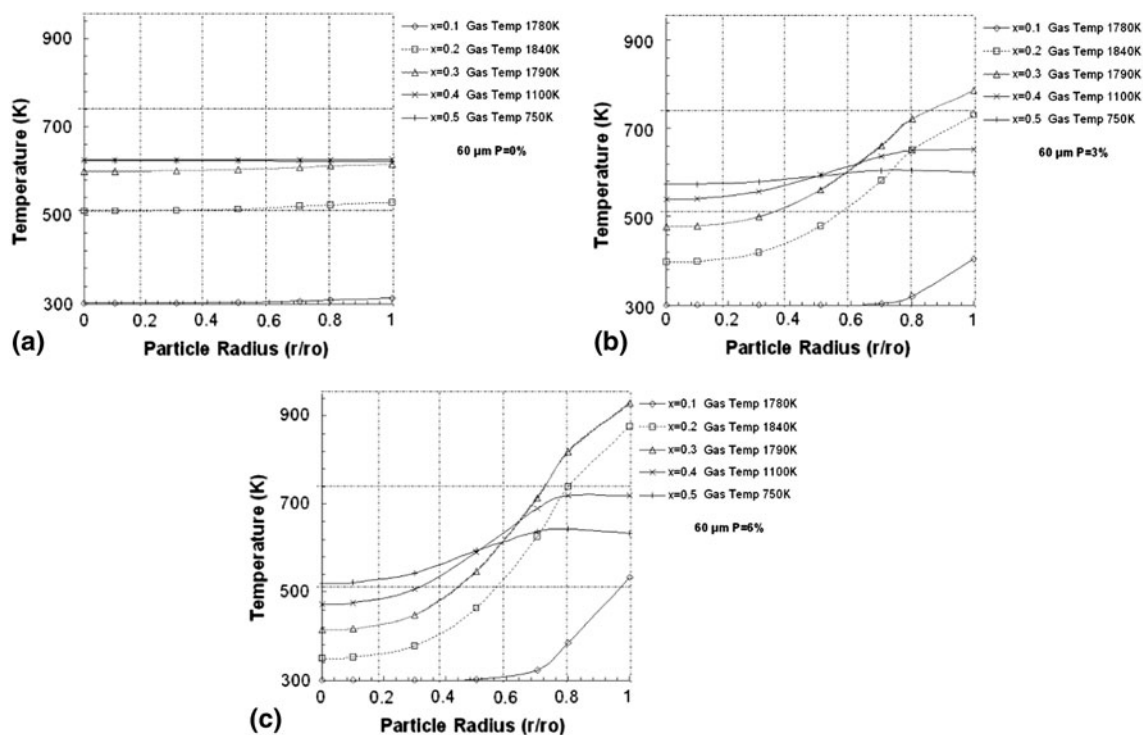


**Fig. 4** Temperature profiles inside 60  $\mu\text{m}$  particle of different porosity

higher surface temperature that exceed 250 K in some cases. This increase in temperature is of great importance for metallic powder which has a lower melting point. The phenomenon needs to be examined carefully and controlled to avoid overheating, oxidation or other issues which affect the quality of coatings. The prediction of large temperature gradient in porous powders is consistent with the finding from experimental study of  $\text{Al}_2\text{O}_3$  powder (Ref 21), where the images for the fracture surfaces of deposited agglomerates of nanoparticles are presented. The outer zones of the particles have undergone melting, liquid phase sintering and solid state sintering, according to the thermal history. The cores of the particles have retained their initial nanostructure.

To examine the influence of porosity on different particle sizes, the temperature profiles are plotted inside the 10, 40, and 60  $\mu\text{m}$  particle of same porosity of  $P=6\%$  in Fig. 5. It is important to mention that the 60  $\mu\text{m}$  particle experiences a very rapid surface heating at  $x=0.1$  m, which results in a surface temperature almost the same as the one of 40  $\mu\text{m}$  at  $x=0.2$  m. Knowing the exact surface temperatures at each point of the particle trajectory, the process control can be optimized by altering the spraying distance in favor of deposition rate increase. Our recent work (Ref 6) has shown that bonding between particles and substrate is attributed mainly to stress localization and melting of the interfacial contact region. It is therefore important to know the temperature in this thin surface region instead of an average particle temperature. Based on the previous calculations of particle surface temperatures and results from previous investigations (Ref 5) the

influence of porosity on deposition efficiency is discussed in the following section.

### 3.3 Porosity Influence on Deposition

Figure 6 is created according to the bonding criterion of adiabatic shear-instability reported in Ref 5. It is necessary to know the critical impact velocities and temperatures for different particle sizes and porous level to obtain adequate bonding strengths. Figure 6 plots the critical velocity as a function of impact temperature for porous powder of 0, 3, and 6% with size 10, 40, and 60  $\mu\text{m}$ , respectively. The points in the cycles represent the particle impact velocities and temperature obtained for different distances from the injection point. For the particles located above the line, the kinetic and thermal energies are adequate to ensure bonding with the substrate. From the range of particles used, only powder sizes smaller than 40  $\mu\text{m}$  have gained enough kinetic and thermal energies to have successful bonding. To address the porosity influence, particles with  $P=6\%$  and size 10  $\mu\text{m}$  are located well above the critical line so the momentum output is sufficient to generate the deformation required for good adhesion. When the size is increased to 40  $\mu\text{m}$  only particles with 6% porosity and reduced impact distance of  $x=0.4$  m lay on the critical line. For lower porosity, all particles are located below the adhesion limit. For 60  $\mu\text{m}$ , the calculated impact values are significantly lower for all porosity levels, indicating that particles of this range cannot be deposited on the substrate.

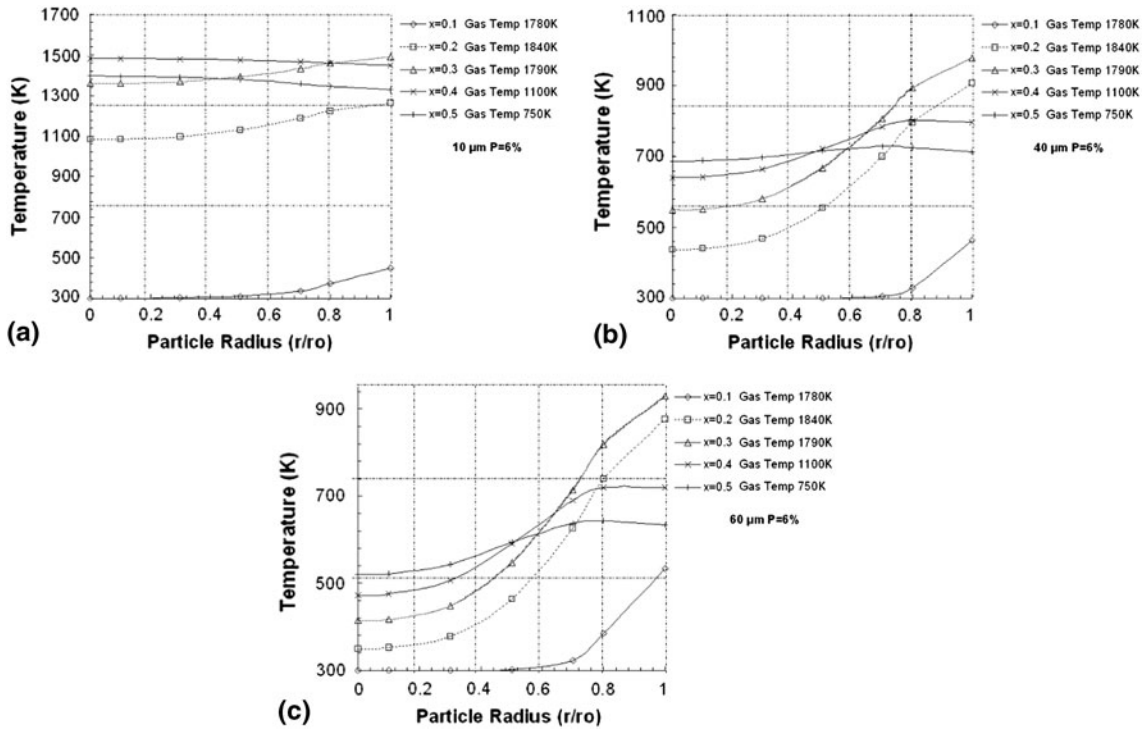


Fig. 5 Temperature profiles inside 10, 40, and 60  $\mu\text{m}$  particles at 6% porosity

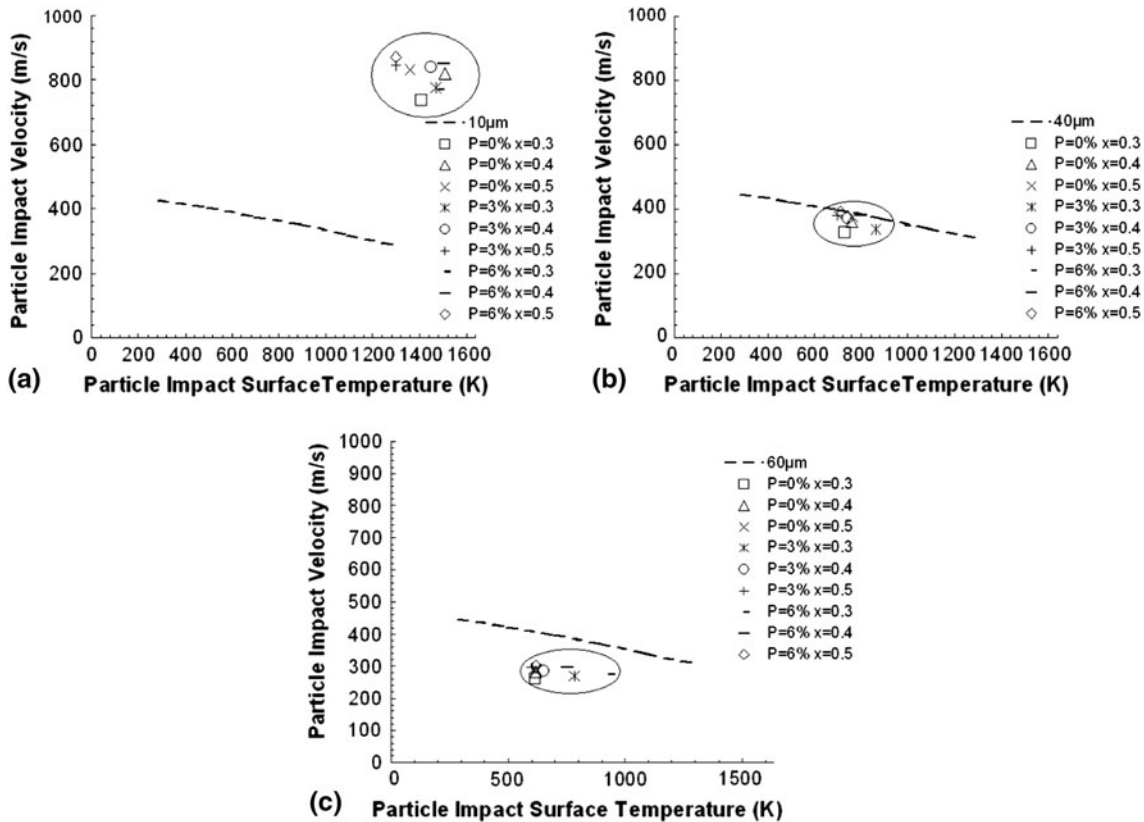
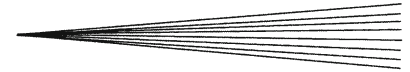


Fig. 6 Critical impact parameters



## 4. Conclusions

Computational model is developed to examine HVOF sprayed porous WC-Co powder. The results indicate that porous particles are accelerated to higher velocity with higher surface temperatures than fully solid powders. Temperature gradient increases with porosity and is more pronounced for large particles. Porous particles at a size range around 40  $\mu\text{m}$  porosity can have improved deposition as a result of combined effect of increased surface temperature and impact velocity. Further increase of porosity level from 6% could give better deposition for particles larger than 40  $\mu\text{m}$ .

## Acknowledgment

The authors gratefully acknowledge the financial support from EU FP7 SIMUSPRAY Project (Grant No. 230715).

## References

1. M. Pasandideh-Fard, S. Chandra, and J. Mostaghimi, A Three-Dimensional Model of Droplet Impact and Solidification, *Int. J. Heat Mass Transfer.*, 2002, **45**, p 2229-2242
2. S. Kamnis and S. Gu, Numerical Modelling of Droplet Impingement, *J. Phys. D*, 2005, **38**, p 3664-3673
3. S. Kamnis, S. Gu, T.J. Lu, and C. Chen, Numerical Modelling of Sequential Droplet Impingements, *J. Phys. D*, 2008, **41**, p 165303-165309
4. W.Y. Li, C. Zhang, X.P. Guo, J.L. Xu, C.J. Li, H. Liao, C. Coddet, and K.A. Khor, Ti and Ti-6Al-4V Coatings by Cold Spraying and Microstructure Modification by Heat Treatment, *Adv. Eng. Mater.*, 2007, **9**, p 418-423
5. S. Gu and S. Kamnis, Bonding Mechanism from the Impact of Thermally Sprayed Solid Particles, *Metall. Mater. Trans. A.*, 2009, **40**, p 2664-2674
6. S. Kamnis, S. Gu, T.J. Lu, and C. Chen, Numerical Modeling the Bonding Mechanism of HVOF Sprayed Particles, *Comp. Mater. Sci.*, 2009, **46**, p 1038-1043
7. M. Li and D. Christofides, Modeling and Control of High-Velocity Oxygen-Fuel (HVOF) Thermal Spray: A Tutorial Review, *J. Therm. Spray Technol.*, 2009, **18**, p 753-768
8. D. Shi, M. Li, and P.D. Christofides, Diamond Jet Hybrid HVOF Thermal Spray: Rule-Based Modeling of Coating Microstructure, *Ind. Eng. Chem. Res.*, 2004, **43**, p 3653-3665
9. S. Gu and S. Kamnis, Numerical Modelling of In-Flight Particle Dynamics of Non-Spherical Powder, *Surf. Coat. Technol.*, 2009, **203**, p 3485-3490
10. M. Li, D. Shi, and P.D. Christofides, Modeling and Control of HVOF Thermal Spray Processing of WC-Co Coatings, *Powder Technol.*, 2005, **156**, p 177-194
11. M. Li and P.D. Christofides, Multi-Scale Modeling and Analysis of an Industrial HVOF Thermal Spray Process, *Chem. Eng. Sci.*, 2005, **60**, p 3649-3669
12. J. Kovacic, The Tensile Behaviour of Porous Metals Made by Gasar Process, *J. Mater. Sci. Lett.*, 1999, **18**, p 1007-1010
13. L. Pawlowski, *The Science and Engineering of Thermal Spray Coatings*, Vol 429, Wiley, Chichester, 1995
14. S.A. Morsi and A.J. Alexander, An investigation of Particle Trajectories in Two-Phase Flow Systems, *J. Fluid Mech.*, 1972, **55**, p 193-200
15. E. Bourdin, P. Fauchais, and M.I. Boulos, Transient Heat Conduction Under Plasma Condition, *Int. J. Heat Mass Transf.*, 1983, **26**, p 567-582
16. V.V. Sobolev and J.M. Guilemany, Dynamic Processes During High Velocity Oxyfuel Spraying, *Int. Mater. Rev.*, 1996, **41**, p 13-32
17. M.C. Flemings, *Solidification Processing*, McGraw-Hill, New York, NY, 1974
18. W.E. Ranz and W.R. Marshall, Evaporation from Drops Part I, *Chem. Eng. Prog.*, 1952, **48**, p 141-150
19. S. Kamnis, S. Gu, T.J. Lu, and C. Chen, Computational Simulation of Thermally Sprayed WC-Co Powder, *Comput. Mater. Sci.*, 2008, **43**, p 1172-1182
20. S. Kamnis and S. Gu, 3-D Modelling of Kerosene-Fuelled HVOF Thermal Spray Gun, *Chem. Eng. Sci.*, 2006, **61**, p 5427-5439
21. D. Zois, A. Lekatou, and M. Vardavoulas, A Microstructure and Mechanical Property Investigation on Thermally Sprayed Nanostructured Ceramic Coatings Before and after a Sintering Treatment, *Surf. Coat. Technol.*, 2009, **204**, p 15-27